Article

Submillimetre hot-electron transport in manganese-doped quantum dot solids

https://doi.org/10.1038/s41586-026-11279-9

Received: 2 April 2026

Accepted: 8 October 2026

Published online: 25 November 2026

Open access

Check for updates

Whi Dong Kim[1,2], Clément Livache[1,3], Ho Jin[1,4], Valerio Pinchetti[1], Tung H. Dang[1], Oleg V. Kozlov[1], Heeyoung Jung[1], Zachary L. Robinson[1] & Victor I. Klimov[1]✉

Colloidal quantum dot solids are promising for photoconversion and photochemistry, but their performance is fundamentally limited by rapid hot-carrier cooling, low carrier mobility and short transport ranges[1]. Here we demonstrate a spin-exchange-driven phototransport regime in manganese-doped quantum dot films that enables the generation, long-range transport and regeneration of hot carriers. Ultrafast spin-exchange-mediated Auger upconversion promotes electrons into high-energy, delocalized states before phonon cooling[2,3], establishing a transient high-mobility conduction channel. Crucially, spin-exchange interactions not only generate hot carriers but also enable their repeated re-excitation, thereby sustaining long-range drift. This mechanism yields room-temperature mobilities of about 150 $cm^2 V^{-1} s^{-1}$ and submillimetre drift lengths—far greater than those of conventional quantum dot solids and approaching values characteristic of crystalline semiconductors. Time-of-flight measurements confirm drift-dominated transport, with transit times scaling linearly with distance and inversely with electric field. These results establish a route to long-range energy transport in nanoscale materials and enable the use of hot carriers in photoconversion, photochemistry and transit-time-limited photodetection.

Photoconversion processes underpin technologies ranging from photodetection and photovoltaics to photoemission and photochemistry. Their ability to exploit excess photon energy is limited by rapid phonon-assisted cooling of nonequilibrium ('hot') carriers to band-edge states, typically within picoseconds, severely restricting their lifetime and transport range. Stabilizing and transporting hot carriers therefore remains a substantial challenge for advanced solar-energy conversion[4–7] and high-energy photochemistry[8,9].

Recent studies have shown that hot carriers can be manipulated using ultrafast spin exchange (SE) interactions in manganese (Mn)-doped colloidal quantum dots (QDs)[10–12]. These interactions mediate subpicosecond Auger-type energy transfer between QD excitons and Mn spin states, reaching energy-transfer rates of about 10 eV ps^{-1} (ref. 11), well above typical phonon-related energy-loss rates ($\lesssim$1 eV ps^{-1})[13,14]. By outcompeting intraband cooling, SE-Auger processes provide an efficient pathway for harvesting hot-electron energy, enabling phenomena such as visible-light generation of solvated electrons[2,15] and carrier multiplication[12].

Here we demonstrate that SE-Auger upconversion in Mn-doped QD films promotes photoelectrons into high-energy, delocalized transport states, enabling rapid, long-range hot-carrier transport through the QD solid. Transient photocurrent (TPC) measurements reveal time-of-flight (ToF) dynamics with drift mobilities of about 150 $cm^2 V^{-1} s^{-1}$ and submillimetre transport distances—well beyond those typically observed in QD solids. These results establish a route to long-range hot-carrier transport for photoconversion and hot-electron-driven photochemistry.

QD samples and Mn-induced SE dynamics

We prepared undoped (reference) and Mn-doped CdSe QDs overcoated with a thin protective CdS shell (Methods). We focus on CdSe/CdS QDs with an initial core radius of $r_{CdSe} \approx 1.65$ nm. The undoped sample exhibits a photoluminescence (PL) peak at about 2.15 eV and a band-edge (1S) absorption feature at about 2.23 eV (Fig. 1a, black curves).

Mn-doped samples were synthesized by diffusion doping of the CdSe cores, involving partial $Cd^{2+} \rightarrow Mn^{2+}$ cation exchange near the surface followed by Mn diffusion into the core interior[16,17] (Methods). The Mn content was controlled by the doping time (t_{Mn} = 5–30 min). Here we examine samples prepared with t_{Mn} = 10 and 20 min, referred to as 'lightly' and 'heavily' doped QDs, respectively.

The lightly doped QDs show spectral features similar to those of the undoped reference (Fig. 1a, blue curves), indicating no appreciable change in the effective CdSe core size. The heavily doped sample exhibits an approximately 130-meV blue shift of both PL and absorption (Fig. 1a, red curves), consistent with a reduction of the effective CdSe core radius to about 1.35 nm owing to formation of a higher-bandgap $Mn_xCd_{1-x}Se$ surface layer.

Mn incorporation strongly modifies single-exciton PL dynamics measured at low excitation levels ($\langle N \rangle < 0.1$, in which $\langle N \rangle$ is the average

[1]Nanotechnology and Advanced Spectroscopy Team, C-PCS, Chemistry Division, Los Alamos National Laboratory, Los Alamos, NM, USA. [2]Present address: Regional Industrial Innovation Department, Korea Institute of Industrial Technology, Cheonan, Republic of Korea. [3]Present address: Laboratoire de Physique de la Matière Condensée, Ecole Polytechnique, CNRS, Institut Polytechnique de Paris, Palaiseau, France. [4]Present address: Department of Chemistry, Ulsan National Institute of Science and Technology, Ulsan, Republic of Korea. ✉e-mail: klimov@lanl.gov

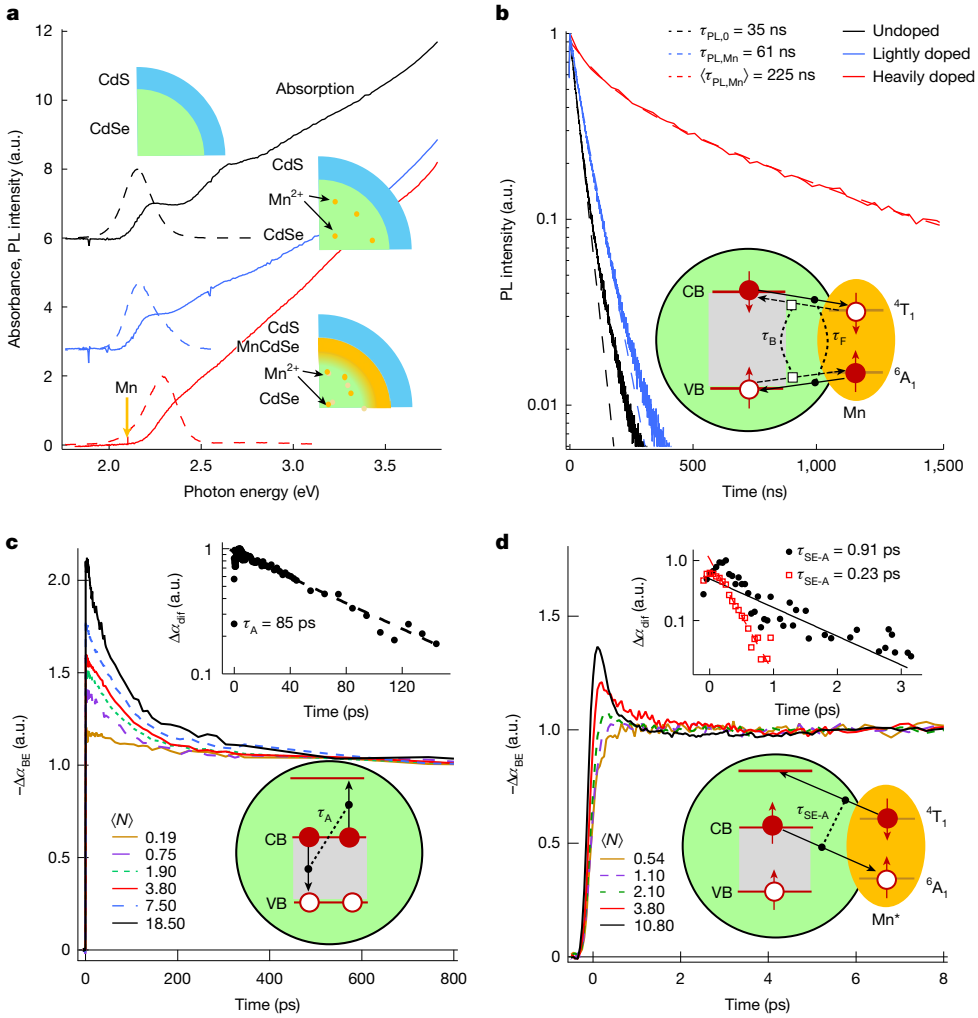

Fig. 1 | Optical properties and exciton dynamics of undoped and Mn-doped QDs. a, Absorption (solid lines) and PL (dashed lines) spectra of undoped (black), lightly doped (blue) and heavily doped (red) QDs. The orange arrow marks the internal Mn spin-flip transition (E_{Mn} = 2.1 eV). Insets, schematics of undoped (top), lightly doped (middle) and heavily doped (bottom) CdSe/CdS QDs. In the heavily doped sample, an interfacial $Mn_xCd_{1-x}Se$ barrier layer forms between the CdSe core and CdS shell. **b**, PL dynamics of undoped (black), lightly doped (blue) and heavily doped (red) QDs. Single-exponential fits to the undoped and lightly doped traces (dashed lines) yield $\tau_{PL,0}$ = 35 ns and $\tau_{PL,Mn}$ = 61 ns, respectively; a double-exponential fit to the heavily doped trace (dashed red line) gives an average lifetime of $\langle\tau_{PL,Mn}\rangle$ = 225 ns. Inset, forward (time constant τ_F, solid black arrows) and backward (τ_B, dashed black arrows) SE-driven excitation transfer between the QD exciton and Mn spin excitation. Short red arrows indicate the spin orientation of electrons (filled red circles); for holes (open red circles), the arrow denotes the spin of the electron removed to create the hole. **c**, Tail-normalized band-edge bleach dynamics of the undoped sample as a function of $\langle N\rangle$, the average number of excitons generated per QD per pulse; $\Delta\alpha_{BE}$ is the pump-induced change in the band-edge absorption coefficient. At $\langle N\rangle \geq 1$, a fast component emerges owing to multiexciton Auger recombination, illustrated in the bottom inset for a biexciton (XX). Top inset, biexciton dynamics obtained by subtracting tail-normalized traces measured at $\langle N\rangle$ = 1.32 and 0.19 (circles); a single-exponential fit (line) gives τ_A = 85 ps. **d**, Corresponding dynamics for lightly doped QDs show strongly accelerated decay owing to SE-Auger recombination (note the 8-ps time window compared with 800 ps in **c**). The SE-Auger lifetimes of hybrid biexciton (X–Mn*) and triexciton (XX–Mn*) states, extracted using the subtraction procedure (top inset), are $\tau_{SE\text{-}A}$ = 0.91 ps and 0.23 ps, respectively. The SE-Auger process is illustrated in the bottom inset. All measurements were performed on QD solutions in toluene; time-resolved PL and TA measurements used 150-fs, 2.4-eV excitation pulses. a.u., arbitrary units.

number of excitons generated per QD per pulse). The PL lifetime increases from $\tau_{PL,0}$ = 35 ns in undoped QDs to $\tau_{PL,Mn}$ = 61 ns in lightly doped QDs and to an average of 225 ns in heavily doped QDs (Fig. 1b).

This behaviour arises from ultrafast (subpicosecond) bidirectional SE-mediated excitation transfer between the QD exciton (X) and the internal Mn spin-flip transition (E_{Mn} = 2.1 eV)[2,10,18]. In the forward process, the QD exciton relaxes while promoting the Mn ion from the spin-up $^6A_1$ ground state to the spin-down $^4T_1$ state (Fig. 1b, inset). This occurs through two concerted spin-conserving transfers: a spin-up Mn 3d electron fills the QD valence-band (VB) hole, while a spin-down QD conduction-band (CB) electron is simultaneously transferred into the Mn 3d shell. In the reverse process, spin-flip relaxation of the excited Mn ion (Mn*) regenerates a QD exciton.

The rapid forward and backward transfers establish a quasi-steady-state distribution between excitonic and Mn-based states, with occupation probabilities p_X and p_{Mn} related by $p_X/p_{Mn} = \exp[-(E_X - E_{Mn})/\delta_0]$, in which E_X is the exciton energy (determined from the PL peak energy) and δ_0 = 103 meV is an experimentally determined characteristic energy[3,11]. Because the intrinsic Mn* lifetime is very long ($\tau_{Mn} \geq 1$ ms; ref. 18), decay of the coupled X–Mn system is governed by its excitonic component, $1/\tau_{PL,Mn} \approx p_X/\tau_{PL,0}$.

For the lightly doped sample, in which $E_{Mn} \approx E_X$, $p_X \approx p_{Mn}$, giving $\tau_{PL,Mn} \approx 2\tau_{PL,0} \approx 70$ ns, close to the measured 61 ns. For the heavily doped sample ($E_X - E_{Mn}$ = 188 meV), the model yields $\tau_{PL,Mn} \approx 7.2\tau_{PL,0} \approx 252$ ns, again close to the observed 225 ns. The prolonged lifetime of the coupled X–Mn excitation facilitates multiexciton formation and

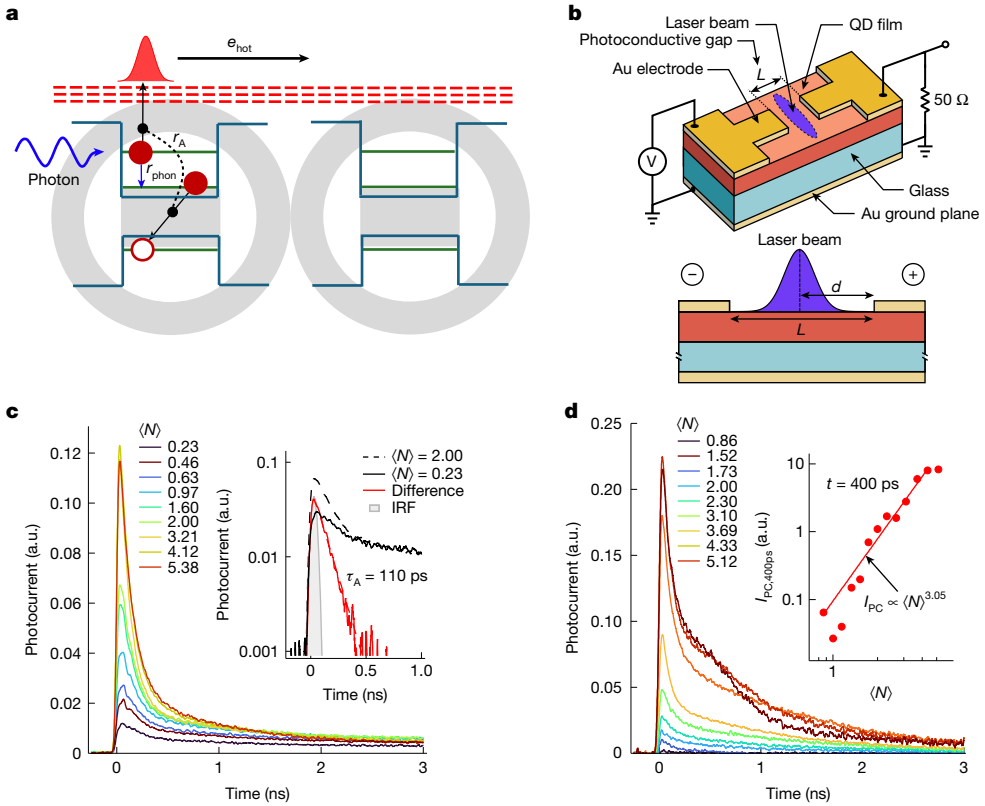

Fig. 2 | Auger-assisted phototransport and TPC measurements of undoped and Mn-doped QDs. a, Schematic of Auger-assisted hot-carrier photoconductance. Absorption of an above-band-edge photon (wavy blue arrow) in a QD containing a pre-existing electron generates a multicarrier (trion) state that undergoes Auger recombination, promoting an electron into a high-energy, delocalized hot state. Access to this state requires retention of the photogenerated electron's excess energy and is therefore efficient only when the Auger energy-transfer rate (r_A) exceeds the phonon-assisted energy-loss rate (r_{phon}). **b**, Schematic of the Auston switch device containing a QD film as the photoactive layer (top) and the experimental geometry (bottom). The QD film within the 70-μm gap (L) between two gold (Au) electrodes is excited by a focused laser beam whose position can be translated across the gap; d denotes the distance between the beam centre and the positive electrode. **c**, Photocurrent transients for the undoped sample as a function of excitation level ($\langle N \rangle$ = 0.23–5.38). Inset, tail-normalized TPC traces for $\langle N \rangle$ = 0.23 and 2.00 (black); their difference (red) is fitted to a single exponential, yielding a biexciton Auger lifetime of τ_A = 110 ps. Measurements used 150-fs, 3.6-eV excitation pulses with the beam centred at d = 15 μm. IRF denotes the instrument response function. **d**, TPC traces for the heavily doped sample under identical conditions exhibit markedly different behaviour at high $\langle N \rangle$, developing a pronounced step-like component whose amplitude increases rapidly—approximately cubically—with $\langle N \rangle$ (inset). a.u., arbitrary units.

thereby supports the SE-Auger processes underlying the long-range hot-electron transport discussed below.

Although slowing single-exciton decay, Mn doping greatly accelerates multiexciton dynamics, which in undoped QDs are governed by Auger recombination, for which electron–hole recombination energy is transferred to a third carrier within the same QD[19] (Fig. 1c, bottom inset). In the undoped sample, this process appears as a fast decay component in transient absorption (TA) traces (Methods), emerging near $\langle N \rangle \approx 1$ (Fig. 1c). From this component, we extract a biexciton Auger lifetime of τ_A = 85 ps (Fig. 1c, top inset).

In Mn-doped QDs, the TA decay also accelerates near $\langle N \rangle \approx 1$ (Fig. 1d, lightly doped sample), but the corresponding time constant is nearly two orders of magnitude shorter, about 910 fs, and decreases further to about 230 fs at higher excitation levels (Fig. 1d, top inset). These subpicosecond dynamics arise from SE-Auger recombination of hybrid multiexciton states comprising intrinsic QD excitons and excited Mn ions[2,3]. In the electron re-excitation pathway (Fig. 1d, bottom inset), two concerted spin-transfer events promote a spin-down Mn 3d electron into a hot QD CB state, whereas the Mn ion is restored to its ground-state configuration by transfer of a spin-up electron from the QD band-edge CB state. As a result, the hot electron is elevated above the QD band edge by E_{Mn}.

Previous studies established that the SE-Auger rate depends mainly on exciton multiplicity and only weakly on the number of excited Mn ions[3]. Accordingly, the observed time constants of 910 and 230 fs are consistent with SE-Auger decay of hybrid biexciton (X–Mn*) and triexciton (XX–Mn*) states, respectively[3].

A key consequence is the very high energy-gain rate associated with SE-Auger upconversion (r_{gain}). For $\tau_{SE\text{-}A}$ = 230 fs, $r_{gain} = r_{SE\text{-}A} = E_{Mn}/\tau_{SE\text{-}A} \approx$ 9 eV ps^{-1}, far exceeding typical phonon-assisted energy-loss rates ($r_{phon} \lesssim 1$ eV ps^{-1})[13,14]. Thus, SE-Auger upconversion can outcompete phonon cooling and efficiently generate and manipulate hot carriers.

TPC and SE-Auger-enhanced transport

A high SE-Auger upconversion rate could enable Auger-assisted hot-carrier transport with strongly enhanced photoconductance. Specifically, theory predicts that Auger excitation above the QD ionization threshold can promote electrons into delocalized, 'quasi-free' states with greatly increased mobility[20]. Experimentally, short-lived bursts of enhanced carrier mobility were previously observed in undoped PbSe QD films[21] and attributed to Auger-generated hot electrons that remained confined within individual QDs. The corresponding transport range was, however, limited to the approximately 50–100-nm near-contact region. Here we use ultrafast SE-Auger interactions to promote electrons above the confinement barrier, as originally foreseen in ref. 20, and show that this enables submillimetre transport.

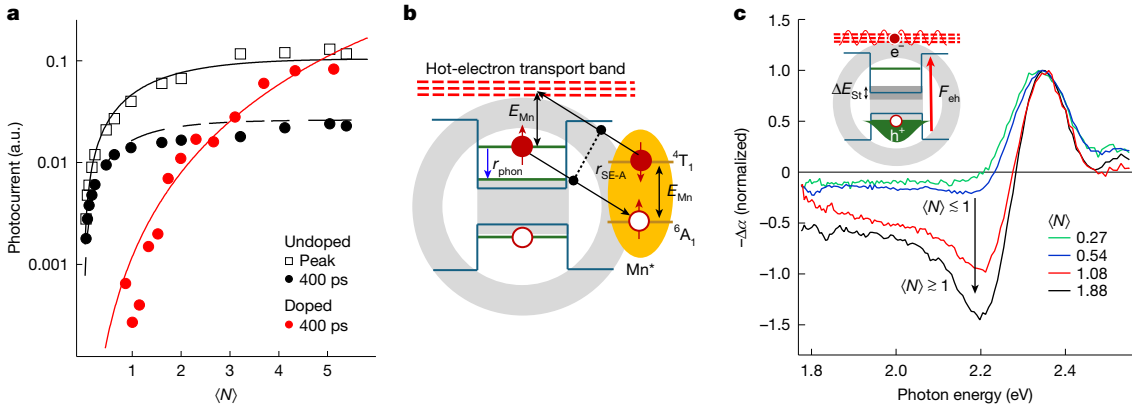

Fig. 3 | TPC and TA evidence for excitation of electrons into peripheral states outside the QD. a, Early-time peak TPC signal (open squares) and long-time (t = 400 ps; post-Auger decay) TPC amplitude (filled black circles) for the undoped sample as a function of $\langle N\rangle$, extracted from Fig. 2c. The data are described by a model assuming Poisson-distributed initial exciton occupancies and constant carrier mobility (black lines). For the doped sample, the TPC step amplitude at t = 400 ps (filled red circles; from Fig. 2d) increases rapidly for $\langle N\rangle > 1$, indicating a strong increase in carrier mobility. The data are reproduced by a model of SE-Auger-assisted activation into a high-mobility hot-electron transport band (red line). **b**, Schematic of SE-Auger upconversion involving an electron in a transient above-band-edge state. This process competes with phonon-assisted relaxation ('cooling') at rate r_{phon}. Efficient promotion of electrons into the hot-carrier transport band requires the SE-Auger energy-transfer rate $r_{SE\text{-}A}$ to exceed r_{phon}. **c**, Early-time TA spectra of a heavily doped QD film (E_{phot} = 3.6 eV, Δt = 3 ps) for $\langle N\rangle \lesssim 1$ (green and blue) and $\langle N\rangle \gtrsim 1$ (red and black). Below the SE-Auger onset, the spectra are dominated by the band-edge bleach from state filling. Above the onset, a pronounced photoinduced absorption develops below the bleach, producing the derivative-like lineshape characteristic of a carrier-induced Stark effect. Inset, SE-Auger activation into a delocalized transport state spatially separates the electron and hole wavefunctions, generating a local electric field (F_{eh}, red arrow) that shifts the band-edge transition by ΔE_{St}. a.u., arbitrary units.

The concept of Auger-enhanced conductivity is illustrated in Fig. 2a. If an electron is excited above the QD confinement barrier—that is, effectively ejected from the QD—it can access a high-mobility transport band formed by closely spaced, delocalized peripheral states[22]. In typical CdSe QDs, however, direct ejection of a band-edge electron by a single conventional Auger upconversion step is unfavourable because the transferred energy, approximately equal to the bandgap E_g, is smaller than the confinement barrier. Ejection can still occur from higher-lying transient states (Fig. 2a) but rapid phonon cooling usually returns carriers to the band edge before Auger upconversion can take place.

Owing to its ultrafast character, SE-Auger upconversion can overcome this limitation by ejecting a nonthermalized electron before it loses its excess energy to phonons[11]. Band-edge electrons can also be expelled from the QD through two sequential SE-Auger upconversion steps[2].

To investigate the role of SE interactions in phototransport, we performed TPC measurements using Auston switch devices in which undoped or Mn-doped QD films were incorporated into a 70-μm gap of a 50-Ω microstrip transmission line[21,23–25] (Fig. 2b and Extended Data Fig. 1; Methods). The QDs were excited by 150-fs laser pulses focused into a narrow stripe (70–80 μm full width at half maximum, FWHM), whose position within the gap was varied by translating the sample. The TPC signal was recorded with a 20-GHz sampling oscilloscope, yielding an overall temporal resolution of approximately 50 ps.

Dark-conductivity measurements (Extended Data Fig. 2) show that the QD films are highly resistive at equilibrium, indicating that the TPC response is dominated by photogenerated rather than equilibrium carriers.

In most experiments, the QDs were excited at E_{phot} = 3.6 eV, more than 1 eV above the band edge. Under these conditions, SE-Auger interactions can efficiently eject electrons from Mn-doped QDs[11], whereas ejection by means of slower conventional Auger processes in undoped QDs is much less likely. Thus, any strong enhancement of photoconductance provides a direct signature of SE-Auger-driven hot-carrier generation and transport.

In Fig. 2c,d, we compare pump-intensity-dependent photocurrent transients for undoped and Mn-doped QD films, respectively, measured at a device bias of V = 100 V and E_{phot} = 3.6 eV.

For the undoped sample, the excitation range corresponds to $\langle N\rangle$ from 0.23 to 5.38 excitons per QD. Increasing pump fluence does not substantially alter the overall TPC profile; the main effect is an acceleration of the early-time decay at $\langle N\rangle \gtrsim 1$, similar to the behaviour observed in TA measurements (Fig. 1c) and likewise indicative of multiexciton Auger recombination. A biexciton Auger lifetime extracted from the fast TPC component (about 110 ps; Fig. 2c, inset) agrees reasonably well with that obtained from TA (about 85 ps; Fig. 1c, inset).

The $\langle N\rangle$ dependence of both the early-time TPC peak amplitude (time $t = t_{peak}$) and the long-time signal (t = 400 ps > τ_A) is also well described by the Auger recombination model (Fig. 3a, black symbols and lines). In this model, the peak photocurrent contains contributions from both single-exciton and multiexciton states, whereas after Auger decay, the long-time signal originates only from single excitons (Supplementary Note 1).

These results show that TPC dynamics in undoped QD films are dominated by carrier recombination, with no detectable signatures of transit across the electrode gap. The corresponding transit times are therefore much longer than the characteristic recombination times because of the low carrier mobility.

In contrast to the undoped samples, photocurrent transients from Mn-doped QD films change markedly with increasing pump fluence (Fig. 2d, heavily doped sample). At $\langle N\rangle \gtrsim 1$, the TPC traces develop a pronounced step-like component whose amplitude grows approximately cubically with $\langle N\rangle$ ($I_{PC,400ps} \propto \langle N\rangle^{3.05}$; Fig. 2d, inset), where $I_{PC,400ps}$ is the photocurrent amplitude measured at t = 400 ps after excitation. This superlinear growth cannot be explained by the increase in carrier population alone and instead indicates an increase in carrier mobility by orders of magnitude.

The onset of this rapid photocurrent growth coincides with the threshold for SE-Auger recombination, suggesting SE-Auger-driven activation of electrons into a higher-energy transport band above the QD confinement barrier, as proposed in ref. 20. The absence of this effect in undoped QDs further points to the critical role of ultrafast SE-Auger upconversion, which can intercept an energetic photoelectron before intraband cooling and promote it into a peripheral, delocalized state outside the QD (Fig. 3b).

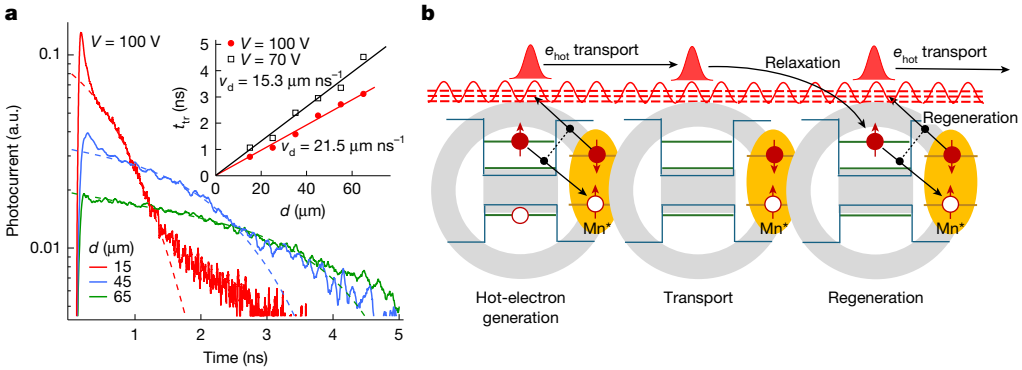

Fig. 4 | ToF transport with SE-Auger generation and regeneration of hot electrons. a, TPC traces for heavily doped QDs measured at $V = 100$ V, $E_{phot} = 3.6$ eV and $\langle N \rangle = 5.12$ (solid lines) for $d = 15$ μm (red), 45 μm (blue) and 65 μm (green). Dashed lines are fits to the ToF model, yielding $v_d = 24$ μm ns^{-1}, 22 μm ns^{-1} and 13 μm ns^{-1}, respectively, with $\tau_0 = 7$ ns. Inset, transit time as a function of d, determined from the inflection points of log–log TPC plots (symbols) for $V = 100$ V (red) and 70 V (black). Linear fits (lines) yield $v_d = 21.5 \pm 0.4$ μm ns^{-1} and 15.3 ± 0.4 μm ns^{-1}, respectively. **b**, Model of hot-electron transport with SE-Auger generation and regeneration. SE-Auger recombination of a hybrid biexciton promotes an electron into a high-mobility transport band above the QD confinement barrier. During drift, the hot electron may partially relax into internal QD states, from which it can be re-excited into the transport band by SE-Auger energy transfer from a long-lived excited Mn ion, sustaining long-range transport. a.u., arbitrary units.

The excitation-level dependence of the TPC step amplitude (evaluated at $t = 400$ ps) further supports its SE-Auger origin. As detailed in Supplementary Note 2, the data are well described using the previously established $(n-1)^2$ scaling of the SE-Auger rate with exciton multiplicity n (Fig. 3a, red symbols and line)[3].

Further evidence for electron ejection from the QD is provided by pump-fluence-dependent TA spectra (Fig. 3c). At $\langle N \rangle < 1$, the spectra are dominated by a state-filling bleach at 2.34 eV, whereas at $\langle N \rangle \geq 1$, they evolve into a derivative-like lineshape characteristic of electron ejection[11,26]. The resulting spatial separation of the ejected electron and the hole remaining in the QD generates an internal electric field (Fig. 3c, inset) that redshifts the band-edge transition through the Stark effect, producing induced absorption below the original bleach.

Fast charge transit in Mn-doped QD films

A step-like TPC signal with an abrupt cut-off is a hallmark of ToF photocurrent observed in high-mobility photoconductors, in which photocarriers are rapidly swept from the photoconductive gap by drift towards the electrodes[27–29]. In this regime, the photocurrent duration is determined not by carrier relaxation but by the carrier transit time, $t_{tr} = d/v_d = d/(\mu F)$, in which d is the transport distance, v_d the drift velocity, μ the carrier mobility and F the electric field.

To test for ToF transport in Mn-doped QD films, we measured photocurrent transients as a function of both transport distance and electric field, $F = V/L$, in which $L = 70$ μm is the electrode gap. Figure 4a shows TPC traces for heavily doped QDs at three distances from the positive electrode, $d = 15$, 45 and 65 μm. The TPC pulse duration increases systematically with d, a defining signature of carrier transit[27] and evidence that the photoresponse is dominated by high-mobility hot electrons generated by SE-Auger upconversion[2,30,31].

The complementary holes remain largely confined within the CdSe cores and are not expected to contribute appreciably to the fast TPC response. However, we do not detect persistent charge accumulation in the photoconductive gap, probably because the non-zero dark conductivity of the QD films (Extended Data Fig. 2) enables charge neutralization between successive excitation pulses.

The measured TPC profiles are well described by the error-function form of the ToF expression for a Gaussian photoexcitation profile (dashed lines in Fig. 4a; Supplementary Note 3 and Extended Data Fig. 3). Minor deviations include an initial capacitive spike[29,32] and a weak long-time tail associated with delayed electrons, discussed below.

Modelling of the $d = 15$ μm trace yields a drift velocity of $v_d = 24$ μm ns^{-1} and an effective lifetime $\tau_0 = 7$ ns. In conventional ToF models, τ_0 describes recombination and/or trapping of mobile carriers. Here it instead represents the effective lifetime of the high-mobility hot-electron population. Whereas hot electrons normally cool to the band edge within a few picoseconds[14,33], in Mn-doped QDs, their lifetime is extended by SE-Auger regeneration (Fig. 4b). Long-lived Mn excitations persist during carrier transit and can repeatedly re-excite partially relaxed electrons into the transport band before complete cooling. Regeneration is imperfect, however: if a relaxing electron encounters a QD lacking an excited Mn ion or otherwise unable to support SE-Auger re-excitation, it relaxes into a low-mobility band-edge state. Thus, τ_0 represents the average survival time of the regenerated hot-electron population.

ToF fits at longer transport distances yield an apparent decrease in v_d from 24 μm ns^{-1} at $d = 15$ μm to 13 μm ns^{-1} at $d = 65$ μm, whereas τ_0 remains essentially unchanged (Fig. 4a). We attribute this reduction to the increasing contribution of delayed electrons that progressively lose mobility as regeneration becomes less effective, broadening the trailing edge of the TPC transient. The shortest-distance value, $v_d = 24$ μm ns^{-1}, therefore provides the best estimate of the intrinsic drift velocity of the regenerated hot-electron population.

We also estimate the transit time with the commonly used empirical approach, in which t_{tr} is identified from the inflection point of a log–log TPC plot, determined from the intersection of power-law fits to the pre-transit and post-transit regions[27,28,34,35] (Fig. 5a). The resulting t_{tr} values scale linearly with d (Fig. 4a, inset), as expected for ToF transport. The slope yields $v_d = 21.5 \pm 0.4$ μm ns^{-1}, in good agreement with the value obtained from error-function modelling of the $d = 15$ μm trace ($v_d = 24$ μm ns^{-1}).

At a lower bias ($V = 70$ V), t_{tr} again scales linearly with d (Fig. 4a, inset and Extended Data Fig. 4), yielding $v_d = 15.3 \pm 0.4$ μm ns^{-1}. The ratio of drift velocities at 70 V and 100 V (0.71) closely matches the voltage ratio (0.7), confirming the expected linear dependence of v_d on electric field. Bias-dependent measurements at fixed distances ($d = 45$ μm and 25 μm; Fig. 5b and Extended Data Fig. 5) provide an independent test: t_{tr} increases with decreasing bias following the expected $1/V$ dependence (Fig. 5c).

Figure 5d summarizes all distance-dependent and bias-dependent measurements (25 data points) by plotting t_{tr} versus d/F, with the horizontal axis scaled by a factor of 10 for convenient unit conversion, as described in the figure caption. For ToF transport, $t_{tr} = d/v_d = (1/\mu)(d/F)$, so the data should follow a straight line with slope $1/\mu$. The experimental data indeed collapse onto a single linear trend (Fig. 5d, black line),

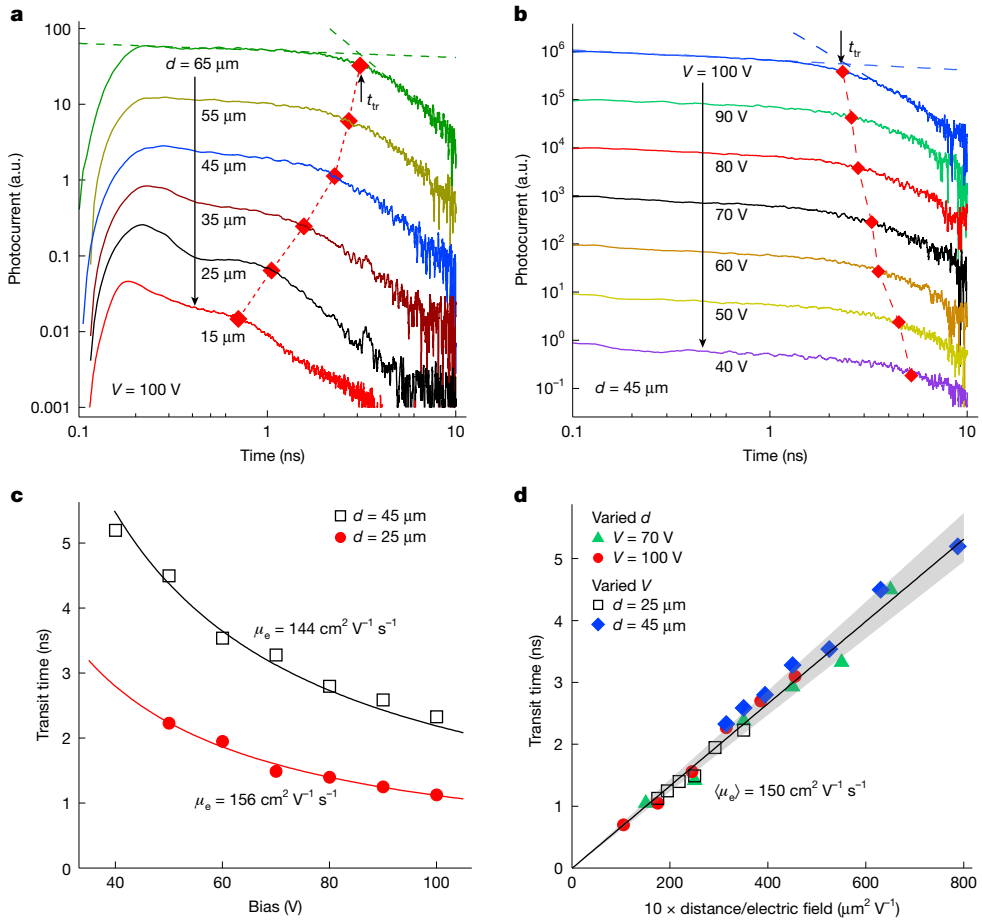

Fig. 5 | Distance-dependent and bias-dependent TPC dynamics and hot-electron drift mobility. a, Log–log plot of distance-dependent TPC traces measured for a heavily doped QD film at $V = 100$ V under 3.6-eV excitation with $\langle N \rangle = 5.12$. The traces are vertically offset for clarity. Straight dashed lines show power-law fits to the pre-transit and post-transit regions of the uppermost TPC trace. Their intersection defines the carrier transit time t_{tr} (red diamonds). **b**, Bias-dependent TPC traces measured at $d = 45$ µm under the same excitation conditions. Carrier transit times determined from the inflection points of the log–log traces are indicated by red diamonds. **c**, Transit time t_{tr} versus bias V for $d = 45$ µm (open black squares) and 25 µm (filled red circles). Fits to $t_{tr} = (1/\mu_e)(dL/V)$ yield electron mobilities of $\mu_e = 144$ cm^2 V^{-1} s^{-1} and 156 cm^2 V^{-1} s^{-1}, respectively. **d**, Transit time versus d/F combining distance-dependent (green and red symbols) and bias-dependent (black and blue symbols) measurements. The d/F axis is multiplied by 10 so that, with t_{tr} in ns and d/F in µm^2 V^{-1}, the slope directly equals $1/\mu_e$ for μ_e expressed in cm^2 V^{-1} s^{-1}. The data follow the expected linear dependence for ToF transport (line), yielding an average electron drift mobility of $\langle \mu_e \rangle = 150 \pm 11$ cm^2 V^{-1} s^{-1}. The shaded region represents the one-standard-error uncertainty of the fitted mobility. a.u., arbitrary units.

yielding an average electron mobility of $\langle \mu_e \rangle = 150 \pm 11$ cm^2 V^{-1} s^{-1}, consistent with values obtained independently from the distance-dependent and bias-dependent data (Fig. 4a, inset and Fig. 5c).

The ToF behaviour is reproducible across independently synthesized QD batches and several Auston switch devices. Further measurements yield electron mobilities of around 150–170 cm^2 V^{-1} s^{-1} (Extended Data Fig. 6), confirming the robustness of the high-mobility hot-electron transport regime.

Although the present study focuses on 3.6-eV excitation, long-range hot-electron transport is also observed under near-band-edge excitation at 2.4 eV (Extended Data Fig. 7). In this case, the onset of the rapid TPC increase shifts from $\langle N \rangle \approx 1$ to $\langle N \rangle \approx 2$, consistent with the SE-Auger ionization model. Because ejection of a near-band-edge electron requires two sequential SE-Auger upconversion steps, ionization occurs only once three excitons are generated, in agreement with previous observations of SE-driven photoionization[2]. Above this threshold, the transport characteristics are essentially unchanged: bias-dependent and distance-dependent TPC measurements exhibit the same ToF behaviour and yield $\langle \mu_e \rangle = 164$ cm^2 V^{-1} s^{-1}, close to the value obtained under 3.6-eV excitation.

The measured drift mobility, $\langle \mu_e \rangle \approx 150$ cm^2 V^{-1} s^{-1}, is about an order of magnitude higher than values typically reported for strongly coupled, device-grade QD films (10–20 cm^2 V^{-1} s^{-1}) (refs. 1,36) and approaches the room-temperature electron drift mobilities of bulk wide-bandgap II–VI semiconductors (approximately 200–600 cm^2 V^{-1} s^{-1}) (ref. 37). This comparison serves only as a benchmark of mobility magnitude and does not imply equivalent transport mechanisms or device operation.

The high hot-electron mobility also enables long transport distances. Using $\tau_0 = 7$ ns and $v_d = 21.5$ µm ns^{-1} ($V = 100$ V) gives a drift range of about 0.15 mm. Such transport distances are extraordinary for colloidal QD solids and place Mn-doped QD films in a transport regime more commonly associated with crystalline semiconductors than with ligand-linked nanocrystal assemblies. Collectively, these results demonstrate a high-mobility transport regime in which SE-Auger excitation promotes photoelectrons into a delocalized hot-carrier transport band, whereas repeated SE-Auger regeneration sustains their long-range drift (Fig. 4b).

Summary

We report a phototransport regime in which SE-Auger upconversion dynamically promotes electrons into a delocalized, high-mobility band above the QD confinement barrier, yielding carrier mobilities of about 150 cm^2 V^{-1} s^{-1} and submillimetre transport distances. Unlike

conventional band-like transport, this mechanism does not rely on miniband formation or strong electronic coupling between neighbouring QDs. Instead, repeated SE-Auger activation regenerates high-energy transport states following partial relaxation, sustaining hot-electron transport over nanosecond timescales.

Long-range hot-electron transport can enable transit-time-limited photodetection in the GHz regime, ultrafast optical-to-electrical signal conversion and modulation and electrical sampling of ultrafast optical signals. Beyond optoelectronics, SE-enabled stabilization and transport of hot carriers offer a strategy for harnessing high-energy electrons in photochemical processes. Their high mobility, expanded wavefunctions and strong reducing power make them attractive as both energetic charge carriers and agents of remote chemical transformations.

Online content

Any methods, additional references, Nature Portfolio reporting summaries, source data, extended data, supplementary information, acknowledgements, peer review information; details of author contributions and competing interests; and statements of data and code availability are available at https://doi.org/10.1038/s41586-026-11279-9.

1. Kagan, C. R., Lifshitz, E., Sargent, E. H. & Talapin, D. V. Building devices from colloidal quantum dots. *Science* **353**, aac5523 (2016).
2. Livache, C. et al. High-efficiency photoemission from magnetically-doped quantum dots driven by multi-step, spin-exchange Auger ionization. *Nat. Photon.* **16**, 433–440 (2022).
3. Pinchetti, V., Jin, H., Livache, C. & Klimov, V. I. Interplay of conventional and spin-exchange Auger recombination in magnetically doped quantum dots. *ACS Nano* **20**, 18999–19014 (2026).
4. Ross, R. T. & Nozik, A. J. Efficiency of hot-carrier solar energy converters. *J. Appl. Phys.* **53**, 3813–3818 (1982).
5. Green, M. A. Third generation photovoltaics: solar cells for 2020 and beyond. *Physica E* **14**, 65–70 (2002).
6. Nozik, A. J. Quantum dot solar cells. *Physica E* **14**, 115–120 (2002).
7. Beard, M. C., Luther, J. M., Semonin, O. E. & Nozik, A. J. Third generation photovoltaics based on multiple exciton generation in quantum confined semiconductors. *Acc. Chem. Res.* **46**, 1252–1260 (2013).
8. Dong, Y., Choi, J., Jeong, H.-K. & Son, D. H. Hot electrons generated from doped quantum dots via upconversion of excitons to hot charge carriers for enhanced photocatalysis. *J. Am. Chem. Soc.* **137**, 5549–5554 (2015).
9. Zhang, Y. et al. Surface-plasmon-driven hot electron photochemistry. *Chem. Rev.* **118**, 2927–2954 (2017).
10. Peng, B., Liang, W., White, M. A., Gamelin, D. R. & Li, X. Theoretical evaluation of spin-dependent Auger de-excitation in Mn^{2+}-doped semiconductor nanocrystals. *J. Phys. Chem. C* **116**, 11223–11231 (2012).
11. Singh, R., Liu, W., Lim, J., Robel, I. & Klimov, V. I. Hot-electron dynamics in quantum dots manipulated by spin-exchange Auger interactions. *Nat. Nanotechnol.* **14**, 1035–1041 (2019).
12. Jin, H., Livache, C., Kim, W. D. & Klimov, V. I. Spin-exchange carrier multiplication in manganese-doped colloidal quantum dots. *Nat. Mater.* **22**, 1013–1021 (2023).
13. Conwell, E. M. *High Field Transport in Semiconductors. Solid State Physics, Supplement 9* (Academic Press, 1967).
14. Klimov, V. I., McBranch, D. W., Leatherdale, C. A. & Bawendi, M. G. Electron and hole relaxation pathways in semiconductor quantum dots. *Phys. Rev. B* **60**, 13740–13749 (1999).
15. Orrison, C. et al. Determination of the generation efficiency and reductive reactivity of the upconverted hot electrons from Mn-doped quantum dots under weak visible light. *J. Am. Chem. Soc.* **147**, 37497–37505 (2025).
16. Vlaskin, V. A., Barrows, C. J., Erickson, C. S. & Gamelin, D. R. Nanocrystal diffusion doping. *J. Am. Chem. Soc.* **135**, 14380–14389 (2013).
17. Jin, H., Goryca, M., Janicke, M. T., Crooker, S. A. & Klimov, V. I. Exploiting functional impurities for fast and efficient incorporation of manganese into quantum dots. *J. Am. Chem. Soc.* **142**, 18160–18173 (2020).
18. Furdyna, J. K. Diluted magnetic semiconductors. *J. Appl. Phys.* **64**, R29–R64 (1988).
19. Klimov, V. I., Mikhailovsky, A. A., McBranch, D. W., Leatherdale, C. A. & Bawendi, M. G. Quantization of multiparticle Auger rates in semiconductor quantum dots. *Science* **287**, 1011–1013 (2000).
20. Shabaev, A., Efros, A. L. & Efros, A. L. Dark and photo-conductivity in ordered array of nanocrystals. *Nano Lett.* **13**, 5454–5461 (2013).
21. Gao, J., Kidon, L., Rabani, E. & Alivisatos, A. P. Ultrahigh hot carrier transient photocurrent in nanocrystal arrays by Auger recombination. *Nano Lett.* **19**, 4804–4810 (2019).
22. Landau, L. D. & Lifshitz, E. M. *Quantum Mechanics: Non-Relativistic Theory, Course of Theoretical Physics* Vol. 3 (Pergamon Press, 1958).
23. Auston, D. H. Impulse response of photoconductors in transmission lines. *IEEE J. Quantum Electron.* **19**, 639–648 (1983).
24. Fidler, A. F., Gao, J. & Klimov, V. I. Electron–hole exchange blockade and memory-less recombination in photoexcited films of colloidal quantum dots. *Nat. Phys.* **13**, 604–610 (2017).
25. Gao, J. B., Fidler, A. F. & Klimov, V. I. Carrier multiplication detected through transient photocurrent in device-grade films of lead selenide quantum dots. *Nat. Commun.* **6**, 8185 (2015).
26. Klimov, V. I. & McBranch, D. W. Auger-process-induced charge separation in semiconductor nanocrystals. *Phys. Rev. B* **55**, 13173–13179 (1997).
27. Kasap, S. O. in *Photoconductivity and Photoconductive Materials: Fundamentals, Techniques and Applications* (ed. Kasap, S. O.) 179–251 (Wiley, 2022).
28. Yazdani, N., Bozyigit, D., Yarema, O., Yarema, M. & Wood, V. Hole mobility in nanocrystal solids as a function of constituent nanocrystal size. *J. Phys. Chem. Lett.* **5**, 3522–3527 (2014).
29. Scher, H. & Montroll, E. W. Anomalous transit-time dispersion in amorphous solids. *Phys. Rev. B* **12**, 2455–2477 (1975).
30. Barrows, C. J. et al. Electrical detection of quantum dot hot electrons generated via a Mn^{2+}-enhanced Auger process. *J. Phys. Chem. Lett.* **8**, 126–130 (2017).
31. Dong, Y., Parobek, D., Rossi, D. & Son, D. H. Photoemission of energetic hot electrons produced via up-conversion in doped quantum dots. *Nano Lett.* **16**, 7270–7275 (2016).
32. Kasap, S. O., Polischuk, B. & Dodds, D. An interrupted field time-of-flight (IFTOF) technique in transient photoconductivity measurements. *Rev. Sci. Instrum.* **61**, 2080–2087 (1990).
33. Klimov, V. I. & McBranch, D. W. Femtosecond 1*P*-to-1*S* electron relaxation in strongly confined semiconductor nanocrystals. *Phys. Rev. Lett.* **80**, 4028–4031 (1998).
34. Noolandi, J. Multiple-trapping model of anomalous transit-time dispersion in a-Se. *Phys. Rev. B* **16**, 4466–4473 (1977).
35. Yoshikawa, T., Nagase, T., Kobayashi, T., Murakami, S. & Naito, H. Analysis of time-of-flight transient photocurrent in organic semiconductors with coplanar-blocking-electrodes configuration. *Thin Solid Films* **516**, 2595–2599 (2008).
36. Kagan, C. R. & Murray, C. B. Charge transport in strongly coupled quantum dot solids. *Nat. Nanotechnol.* **10**, 1013–1026 (2015).
37. Yang, X., Xu, C. & Giles, N. C. Intrinsic electron mobilities in CdSe, CdS, ZnO, and ZnS and their use in analysis of temperature-dependent Hall measurements. *J. Appl. Phys.* **104**, 073727 (2008).

Publisher's note Springer Nature remains neutral with regard to jurisdictional claims in published maps and institutional affiliations.

Open Access This article is licensed under a Creative Commons Attribution-NonCommercial-NoDerivatives 4.0 International License, which permits any non-commercial use, sharing, distribution and reproduction in any medium or format, as long as you give appropriate credit to the original author(s) and the source, provide a link to the Creative Commons licence, and indicate if you modified the licensed material. You do not have permission under this licence to share adapted material derived from this article or parts of it. The images or other third party material in this article are included in the article's Creative Commons licence, unless indicated otherwise in a credit line to the material. If material is not included in the article's Creative Commons licence and your intended use is not permitted by statutory regulation or exceeds the permitted use, you will need to obtain permission directly from the copyright holder. To view a copy of this licence, visit http://creativecommons.org/licenses/by-nc-nd/4.0/.

© The Author(s) 2026

Methods

Materials

Cadmium oxide (CdO, 99.99%, Aldrich), octadecylphosphonic acid (ODPA, 99%, PCI), trioctylphosphine oxide (TOPO, 99%, Aldrich), trioctylphosphine (TOP, 97%, Aldrich), diphenylphosphine (DPP, 98%, Aldrich), selenium (Se, 200 mesh, 99.999%, Alfa Aesar), 1-octadecene (ODE, 90%, Aldrich), oleic acid (OA, 90%, Aldrich), oleylamine (OAm, 70%, Aldrich), manganese(II) acetate tetrahydrate ($Mn(ac)_2{\cdot}4H_2O$, 99.999%, Strem) and tributylphosphine (TBP, 95%, Aldrich) were used as received.

Synthesis of Mn-doped core/shell CdSe/CdS QDs

Synthesis of CdSe cores. CdSe core particles with a wurtzite crystal structure were synthesized following a previously reported method[17]. Specifically, 100 mg of CdO, 490 mg of ODPA and 5 g of TOPO were loaded into a three-neck flask and degassed under vacuum at 150 °C for 1 h. Under nitrogen flow, the mixture was heated to 320 °C and maintained at this temperature until it formed a clear solution. Subsequently, 1 ml of TOP was swiftly injected into the flask. After the temperature increased to 380 °C, 1 ml of a 1.4 M TOP–Se solution was rapidly injected. At this stage, 1 mol% of DPP was added to the TOP–Se solution to control the growth kinetics[17]. After 3 min, the reaction mixture was cooled to room temperature by removing the heating mantle.

The resulting nanocrystals were collected by adding ethanol followed by centrifugation at 8,000 rpm. This washing procedure was repeated three times. The purified nanocrystals were then redispersed in toluene.

Mn doping. To incorporate Mn into the synthesized CdSe nanocrystals, we used a diffusion-doping procedure[16] following a refined protocol of ref. 17. To remove residual Cd species, the pre-synthesized CdSe nanocrystals dispersed in toluene were precipitated with ethanol. 75 mg of the precipitate was dissolved in a mixture of 27 ml of degassed ODE and 2.7 ml of OA. The mixture was heated to 60 °C under vacuum for 1 h. After cooling to room temperature, the nanocrystals were again precipitated with ethanol and collected by centrifugation at 8,000 rpm. The resulting precipitate was added to a mixture of 510 mg of Se, 3 ml of degassed ODE and 3 ml of TBP.

Separately, 90 mg of $Mn(ac)_2{\cdot}4H_2O$, 45 ml of ODE, 1.8 ml of OA and 3.9 ml of OAm were loaded into a flask and degassed under vacuum at 100 °C for 1 h. Under nitrogen flow, the mixture was heated to 300 °C, after which the previously prepared CdSe nanocrystal/TBP–Se solution in ODE was swiftly injected. The reaction temperature was maintained at 300 °C and the doping level was controlled by the reaction time (typically 5–30 min). After completion of the reaction, the mixture was cooled to room temperature. Magnetic circular dichroism measurements indicated approximately 2–5 internal Mn^{2+} dopants per QD, depending on the doping time[17].

CdS shell growth. Owing to the large abundance of surface trap states, as-prepared Mn-doped CdSe cores do not exhibit detectable PL. To suppress surface defects, the cores were coated with a CdS shell following procedures reported in ref. 17.

To prepare a Cd-oleate precursor solution, 123 mg of CdO, 2.45 ml of OA and 10.8 ml of ODE were loaded into a flask and degassed at 100 °C under vacuum for 1 h. Under nitrogen flow, the temperature was increased to 250 °C and maintained for 1 h until a clear solution formed. The precursor solution was then cooled to 100 °C and maintained at this temperature until injection during CdS shell growth.

A TOP–S precursor solution was prepared by stirring a mixture of 18 ml of TOP and 44.3 mg of sulfur powder overnight in a glovebox.

For shell growth, 75 mg of Mn-doped CdSe QDs were dissolved in a mixture of 28 ml of ODE, 2.4 ml of OAm and 1.2 ml of OA. This mixture was degassed at 100 °C under vacuum for 1 h. Under nitrogen flow, the flask was heated to 220 °C and 0.4-ml aliquots of the Cd-oleate and TOP–S precursor solutions were alternately injected dropwise at intervals of 2.5 min for two cycles.

Fabrication of Auston switch devices

A 100-nm gold layer was evaporated onto the backside of a 1-mm glass substrate to serve as the ground plane. An approximately 200-nm-thick film of undoped (reference) or Mn-doped CdSe/CdS QDs was then deposited on the top surface of the substrate through repeated spin-coating cycles, accompanied by ligand exchange and rinsing steps. During deposition, QDs dispersed in octane (20 mg ml^{-1}) were spin-coated at 1,600 rpm for 30 s.

To facilitate interdot charge transport, the QDs were cross-linked by means of solid-state ligand exchange, replacing the original long-chain ligands with short bifunctional 1,2-ethanedithiol (EDT) molecules. For ligand exchange, 60 µl of a 1 M EDT solution in methanol (MeOH) was dropped onto the QD layer, allowed to soak for 60 s and then spin-coated at 1,200 rpm for 30 s.

The film was subsequently rinsed by spin-coating pure MeOH to remove excess ligands. These three steps—QD deposition, ligand exchange and rinsing—were repeated five times to obtain a QD layer approximately 200 nm thick. The resulting film was annealed at 150 °C for 30 min.

Finally, two 200-nm-thick gold contacts separated by a 70-µm gap were deposited on top of the QD film through a shadow mask. Together with the gold ground plane on the backside of the substrate, these contacts form a microstrip transmission line with a nominal impedance of 50 Ω.

To verify that ligand exchange and film fabrication preserved the quantum-confined electronic structure of the QDs, we performed further TA measurements on 200-nm-thick Mn-doped CdSe/CdS QD films prepared using the same ligand-exchange procedure as used for the TPC devices. The TA spectra of the film samples were compared with those of the corresponding QDs in solution under identical excitation conditions (3.6-eV, 150-fs excitation; $\langle N \rangle = 0.3$). The results are presented in Extended Data Fig. 8.

To characterize the equilibrium electrical properties of the ligand-exchanged QD films, further dark-conductivity measurements were performed using 120-nm-thick Mn-doped CdSe/CdS QD films deposited on glass substrates and contacted by thermally evaporated interdigitated Au electrodes comprising 25 pairs of 2-mm-long fingers separated by 10 µm. The corresponding current–voltage characteristics are presented in Extended Data Fig. 2.

Electrostatic simulations of the Auston switch geometry were performed using the Electrostatics interface of COMSOL Multiphysics to calculate the electric-field distribution, effective gap capacitance and effective RC constant (Extended Data Fig. 1).

TA measurements

TA measurements were performed using a standard pump–probe set-up in which absorption changes induced by a short pump pulse were probed in both the temporal and spectral domains using variably delayed probe pulses. The TA system was built around a regeneratively amplified ytterbium-doped potassium gadolinium tungstate (Yb:KGW) femtosecond laser (PHAROS, Light Conversion) generating approximately 190-fs pulses at 1.2 eV.

The laser output was split into two beams. One beam seeded a harmonic generator (HIRO HHG, Light Conversion) to produce second (2.4-eV) or third (3.6-eV) harmonic pump pulses, whose duration was shortened to about 150 fs owing to nonlinear optical pulse compression. Pulses from the second beam were delayed relative to the pump using an optical delay line (up to 5 ns) and focused onto a 3-mm-thick sapphire plate to generate broadband probe pulses in the form of a femtosecond white-light continuum.

The pump beam was focused onto the sample into a spot with a diameter of about 120 µm, whereas the smaller-diameter probe

beam (<90 μm) was centred near the middle of the pump spot. Probe pulses transmitted through the sample were detected using an Avantes AvaSpec-Fast ULS1350F-USB2 spectrometer. The measured TA spectra were corrected for chirp (spectrally dependent delay within the white-light continuum probe pulses) using the procedure described in ref. 2.

In Auger recombination studies of undoped and Mn-doped QDs, we monitored the pump-induced band-edge absorption bleach ($\Delta\alpha_{BE}$), which tracks the decay of band-edge excitonic populations[14].

TPC measurements

To minimize sample degradation during TPC measurements, the fabricated Auston switch devices were mounted in a nitrogen-filled, airtight chamber equipped with optical windows and electrical feedthroughs. Under these conditions, no measurable changes in the TPC response were observed during the complete characterization of a device, including pump-fluence-dependent, transport-distance-dependent and bias-dependent measurements.

The chamber was mounted on a translation stage, allowing the laser beam position within the electrode gap to be varied. One of the top gold electrodes was biased using a DC power supply (Keithley 2430), whereas the other electrode was connected to a 20-GHz-bandwidth sampling oscilloscope by means of a coaxial cable. To minimize timing jitter, the oscilloscope was triggered by electrical pulses generated by a high-speed Si photodetector driven by a portion of the laser beam split from the excitation path.

The QDs within the photoconductive gap of the Auston switch were excited at 2.4 eV or 3.6 eV using 150-fs pulses of the second or third harmonic of an amplified Yb:KGW femtosecond PHAROS laser, respectively. The laser beam was focused with a cylindrical achromatic lens into a narrow stripe aligned with the edges of the top gold electrodes. The spatial profile of the excitation beam was approximately Gaussian, with a stripe width of about 70–80 μm (FWHM), measured with a beam profiler. The excitation position within the photoconductive gap of the Auston switch was varied by translating the sample in a plane perpendicular to the laser beam. The position was initially calibrated using a beam profiler and monitored in real time on the sample with a CMOS camera.

As discussed in Supplementary Note 3, the nonlinear dependence of SE-Auger upconversion on excitation density narrows the lateral spatial profile of the mobile hot-electron population relative to the laser beam profile (Extended Data Fig. 9). Across the film thickness, the initial hot-electron population is weighted towards the illuminated surface. However, because the optical absorption length is comparable with the QD film thickness, excited Mn ions are generated throughout the layer. Consequently, SE-Auger regeneration remains active across the film thickness, even if the hot-electron population spreads vertically during transit within the photoconductive gap.

Data availability

Source data are provided with this paper.

Author contributions V.I.K. conceived the study, analysed the data, modelled the photocurrent transients and wrote the manuscript, with input from all co-authors. H. Jin synthesized the QDs and performed their microstructural characterization. W.D.K. and H. Jung fabricated the Auston switch devices. T.H.D. performed electrostatic modelling of the devices and dark current–voltage measurements. W.D.K. and C.L. performed and analysed the TPC measurements. O.V.K., V.P. and Z.L.R. performed and analysed the ultrafast TA measurements.

Funding Ultrafast optical spectroscopic measurements, TPC studies of QD films and phototransport modelling were supported by the Photochemistry and Radiation Chemistry Program of the Chemical Sciences, Biosciences, and Geosciences Division, Office of Basic Energy Sciences, Office of Science, US Department of Energy. QD synthesis, microstructural characterization and steady-state optical and magneto-optical spectroscopic studies were supported by the Laboratory Directed Research and Development (LDRD) programme at Los Alamos National Laboratory under project no. 20250126DR.

Competing interests The authors declare no competing interests.

Additional information
Supplementary information The online version contains supplementary material available at https://doi.org/10.1038/s41586-026-11279-9.
Correspondence and requests for materials should be addressed to Victor I. Klimov.
Peer review information *Nature* thanks the anonymous reviewers for their contribution to the peer review of this work. Peer reviewer reports are available.
Reprints and permissions information is available at http://www.nature.com/reprints.

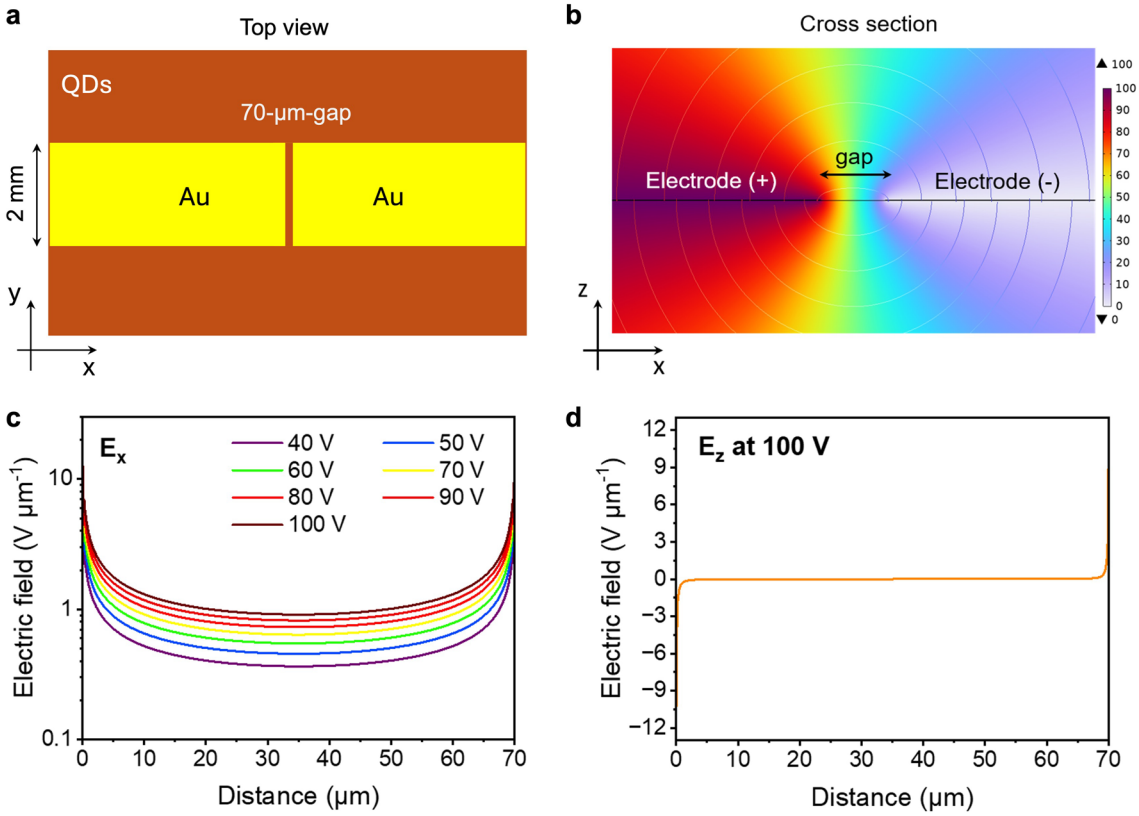

Extended Data Fig. 1 | Electrostatic modelling of the Auston switch device. **a**, Top view of the modelled structure consisting of a 200-nm-thick Mn-doped QD film deposited on a 1-mm-thick glass substrate with two 2-mm-wide and 200-nm-thick gold (Au) electrodes separated by a 70-μm gap. The static dielectric constants of the QD film and glass substrate were taken as 6.0 and 4.1, respectively. **b**, Cross-sectional view showing the calculated electrostatic potential (colour map) and electric-field lines for an applied bias of $V = 100$ V, obtained using the Electrostatics module of COMSOL Multiphysics. **c**,**d**, Calculated horizontal (E_x) and vertical (E_z) electric-field components in the QD film as a function of the distance from the positive electrode. The vertical electric field is negligible over nearly the entire photoconductive gap and becomes appreciable only within approximately 1 μm of the electrode edges. By contrast, the horizontal electric field remains nearly uniform across the gap, with an average value within 10–15% of the nominal field $F = V/L$. These calculations confirm that the electric field is predominantly horizontal, thereby validating the one-dimensional drift approximation used in the charge transport analysis. The computed electrostatic field distribution yields an effective gap capacitance of approximately 0.2 pF, corresponding to an estimated RC time constant of 10 ps for a 50-Ω transmission line. This value is shorter than the experimental temporal resolution of the TPC measurements (about 50 ps), indicating that the measured response is limited not by the device RC constant but by other components of the measurement circuit and the oscilloscope.

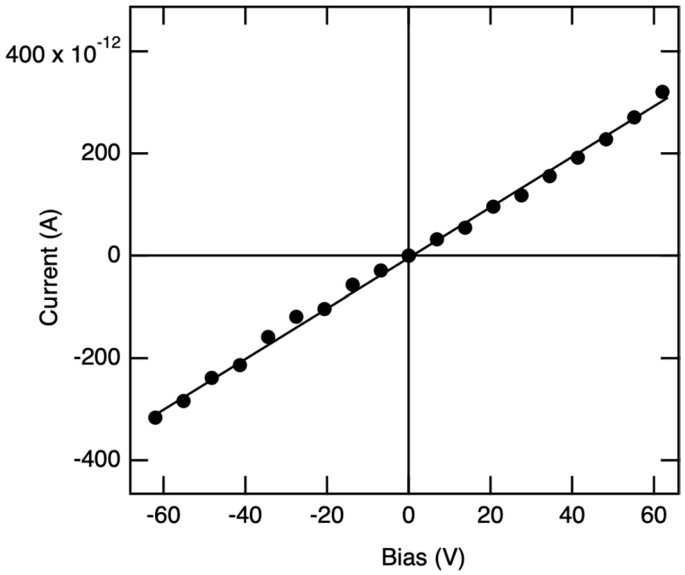

Extended Data Fig. 2 | Dark current–voltage characteristics of ligand-exchanged Mn-doped CdSe/CdS QD films. The measurements were performed on a 120-nm-thick Mn-doped CdSe/CdS QD film deposited on a glass substrate and contacted by thermally evaporated interdigitated Au electrodes comprising 25 pairs of 2-mm-long fingers separated by 10 μm. The measured current exhibits a linear dependence on the applied bias over the investigated voltage range (±60 V), corresponding to maximum electric fields of approximately 6 V μm^{-1}, about four times larger than those used in the TPC experiments. The absence of measurable nonlinearity indicates no detectable contact-limited (Schottky) behaviour under these conditions. The extracted film resistivity is approximately 2.2×10^{10} Ω cm, demonstrating that the ligand-exchanged QD films are highly insulating at equilibrium and therefore contain only a negligible concentration of free carriers.

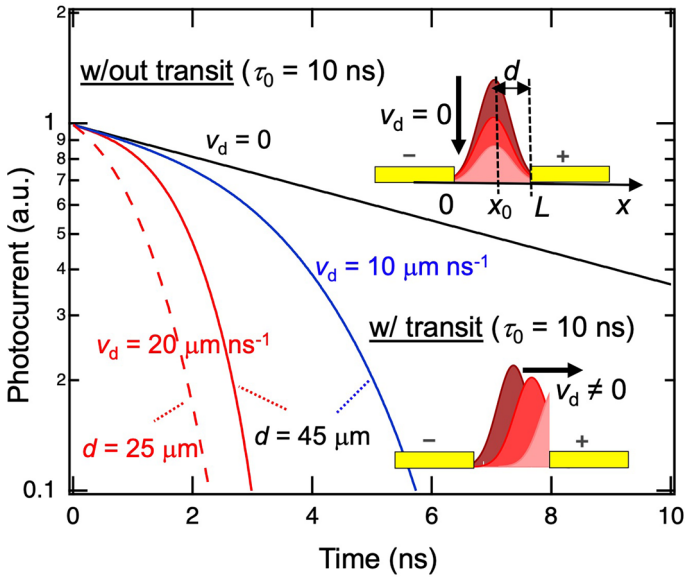

Extended Data Fig. 3 | Modelling of ToF carrier transport. Simulated photocurrent transients for a Gaussian spatial distribution of photogenerated carriers, using an effective lifetime of $\tau_0 = 10$ ns for illustration. In the absence of charge transit ($v_d = 0$, black line; top inset), the photocurrent decays only through carrier loss with time constant τ_0. For a non-zero drift velocity (bottom inset), the transient develops a cut-off when the carrier packet reaches the collecting electrode (the positive contact in the present case, assuming electron-dominated photocurrent). Blue and red traces correspond to $v_d = 10$ μm ns^{-1} and $d = 45$ μm (blue line), $v_d = 20$ μm ns^{-1} and $d = 45$ μm (solid red line) and $v_d = 20$ μm ns^{-1} and $d = 25$ μm (dashed red line). Here d is the distance from the centre of the initial carrier distribution to the charge-collecting electrode and v_d is the drift velocity. a.u., arbitrary units.

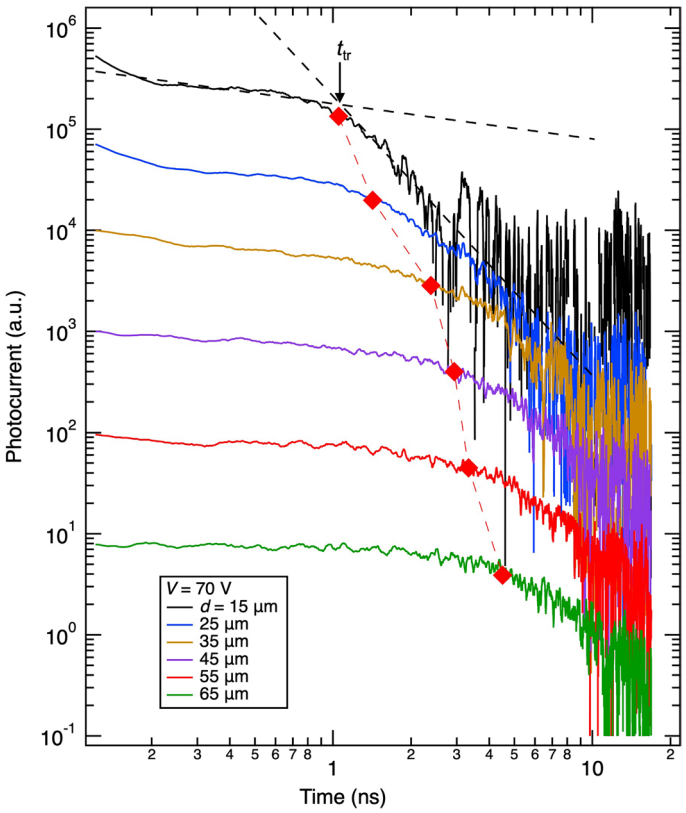

Extended Data Fig. 4 | Further transport-distance-dependent TPC measurements of a heavily doped Mn:CdSe/CdS QD film. TPC traces measured as a function of the transport distance from the positive electrode (d) at a fixed applied bias of 70 V (solid lines) under 3.6-eV, 150-fs excitation at an excitation level of $\langle N \rangle = 5.12$. Dashed straight lines show power-law fits to the pre-transit and post-transit regions of the top TPC trace. The intersection of these lines defines the carrier transit time (t_{tr}), indicated by red diamonds. a.u., arbitrary units.

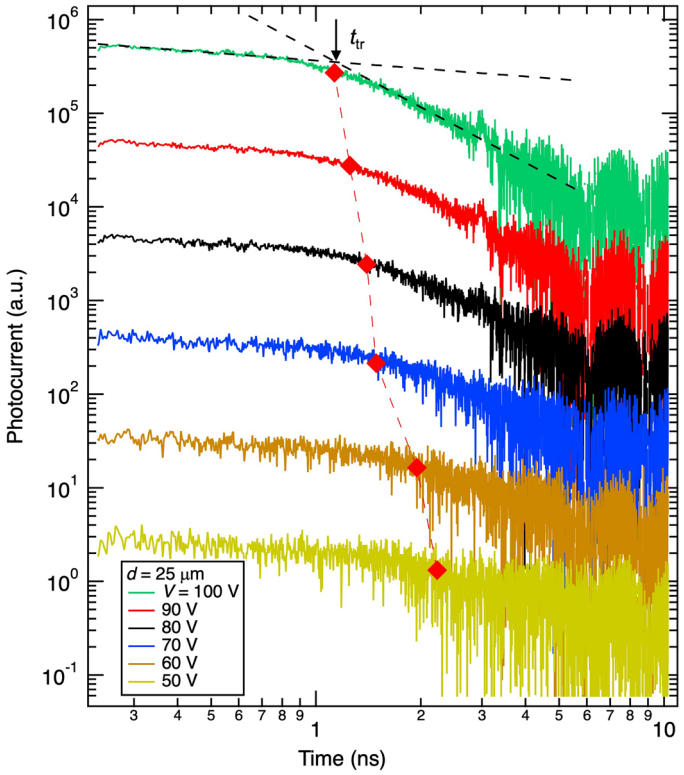

Extended Data Fig. 5 | Further bias-dependent TPC measurements of a heavily doped Mn:CdSe/CdS QD film. TPC traces measured at a fixed transport distance of $d = 25$ μm under 3.6-eV, 150-fs excitation at an excitation level of $\langle N \rangle = 5.12$ (solid lines). Carrier transit times (t_{tr}), determined from the inflection points of the log–log TPC traces, are indicated by diamonds. The inflection points were obtained from the intersections of power-law fits to the pre-transit and post-transit regions (dashed black lines). a.u., arbitrary units.

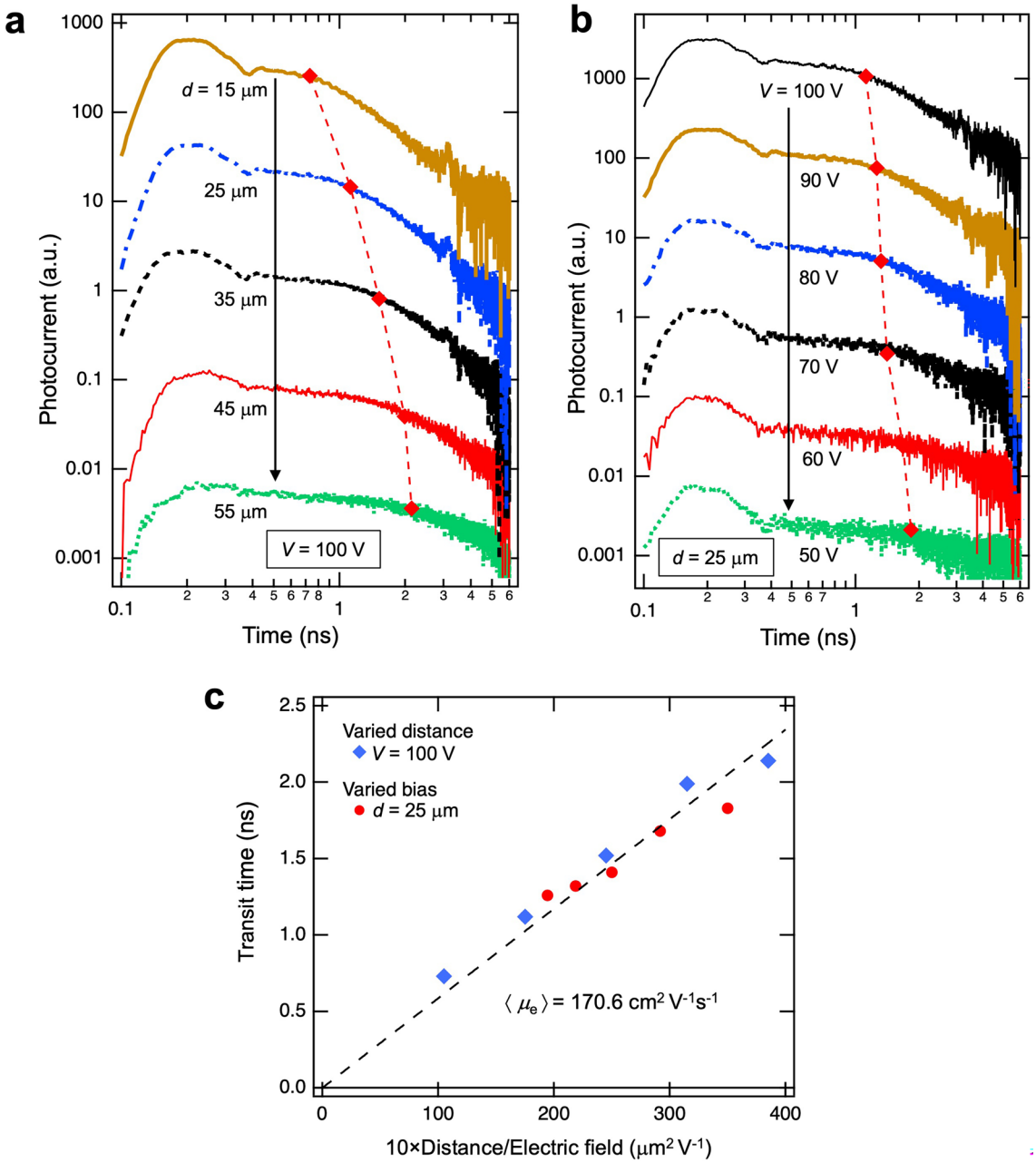

Extended Data Fig. 6 | Reproducibility of the ToF transport regime in an independently prepared Mn-doped QD sample. An extra batch of Mn-doped CdSe/CdS QDs was synthesized independently, incorporated into a separate Auston switch device and measured using excitation with 150-fs, 3.6-eV laser pulses at $\langle N \rangle \approx 5$. **a**, Distance-dependent TPC traces recorded at $V = 100$ V. The carrier transit time (t_{tr}, indicated by red diamonds) increases with the transport distance (d), as expected for ToF transport. **b**, Bias-dependent TPC traces measured at $d = 25$ μm. The measured transit time increases with decreasing V, again consistent with ToF transport. **c**, Transit time plotted as a function of $10d/F$, in which F is the applied electric field, using the data from panels **a** (blue diamonds) and **b** (red circles). The factor of 10 is introduced for convenient conversion of the fitted slope to mobility in $cm^2 V^{-1} s^{-1}$, as described in Fig. 5d. The linear fit (dashed line) yields an average electron mobility of $\langle \mu_e \rangle = 170.6\ cm^2 V^{-1} s^{-1}$, consistent with the value reported in the main text (Fig. 5d). a.u., arbitrary units.

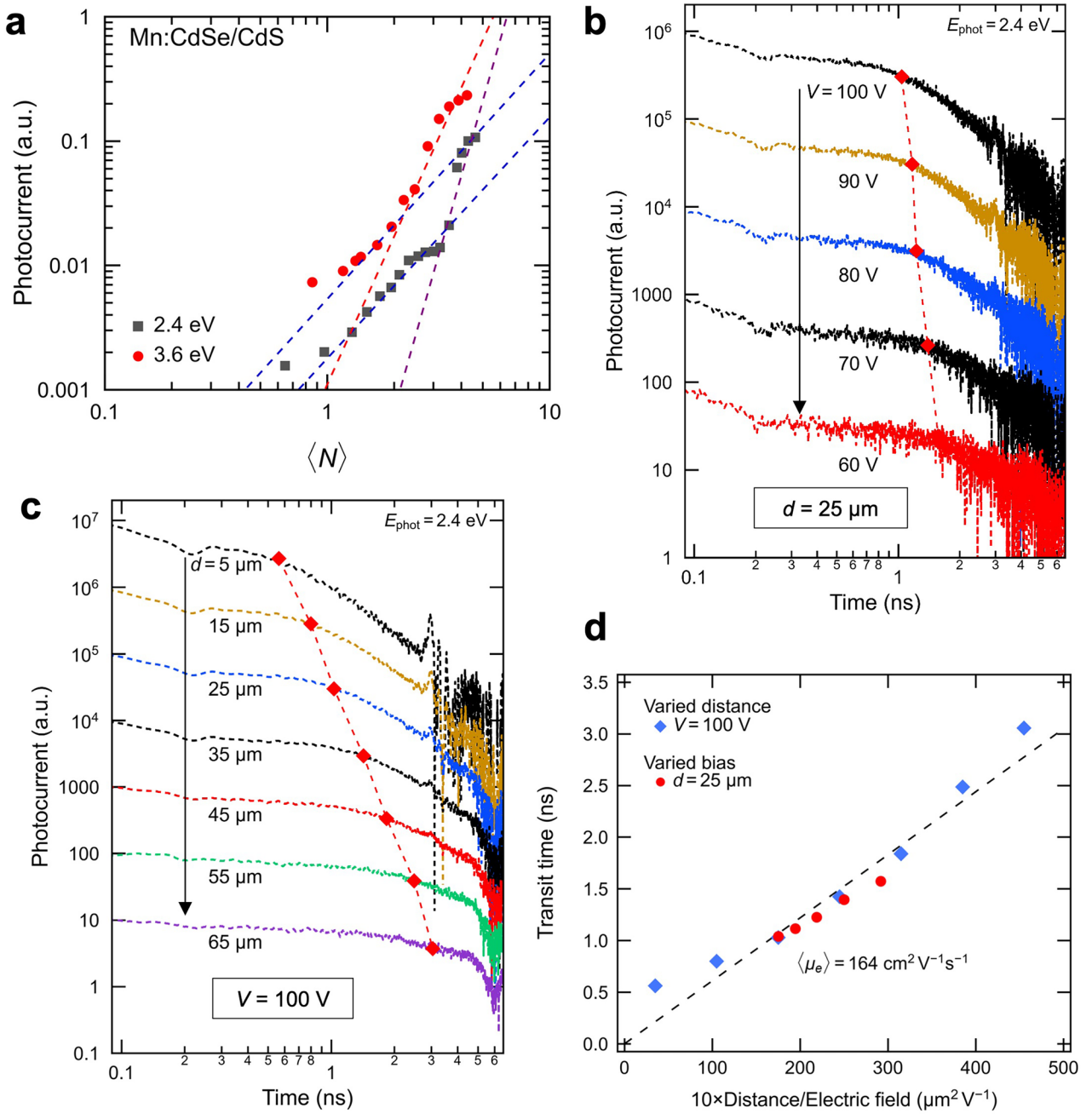

Extended Data Fig. 7 | Long-range hot-electron transport under near-band-edge excitation (photon energy E_{phot} = 2.4 eV). a, Early-time TPC amplitude as a function of the average number of excitons per QD, ⟨*N*⟩, measured using 2.4-eV, 150-fs excitation pulses (black squares). For comparison, corresponding data obtained with 3.6-eV excitation are shown by red circles. The onset of the rapid TPC increase shifts from ⟨*N*⟩ ≈ 1 for 3.6-eV excitation to ⟨*N*⟩ ≈ 2 for 2.4-eV excitation, consistent with hot-electron generation by means of single-step and two-step SE-Auger upconversion, respectively. This behaviour is expected because ejection of a cold band-edge electron requires an energy of approximately 3.5 eV, which exceeds the energy released in a single SE-Auger event (about 2.1 eV) and therefore requires two sequential SE-mediated upconversion steps. **b**, Bias-dependent TPC traces (log–log representation) measured at a fixed transport distance of *d* = 25 μm and ⟨*N*⟩ ≈ 4. Carrier transit times (t_{tr}), determined from power-law fits to the pre-transit and post-transit regions, are indicated by the red diamonds. **c**, Distance-dependent TPC traces measured at an applied bias of 100 V. Transit times are indicated by the red diamonds. **d**, Transit time plotted as a function of 10 *d*/*F*, in which *F* is the applied electric field, obtained from the data in panels **b** (red circles) and **c** (blue diamonds). The factor of 10 is introduced for convenient conversion of the fitted slope to mobility in cm² V⁻¹ s⁻¹, as described in Fig. 5d. The linear fit (line) yields an average electron mobility of ⟨μ_e⟩ = 164 cm² V⁻¹ s⁻¹, demonstrating that long-range, high-mobility transport is preserved under near-band-edge excitation. a.u., arbitrary units.

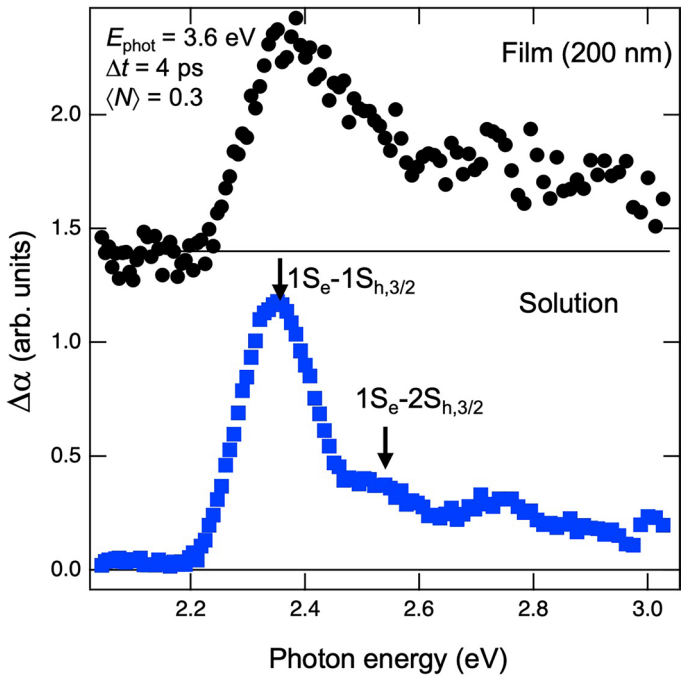

Extended Data Fig. 8 | Preservation of quantum confinement in Mn-doped QD films after ligand exchange and film fabrication. Comparison of early-time TA spectra of Mn-doped CdSe/CdS QDs measured in solution (1-mm optical path length) and in a 200-nm-thick solid-state film prepared using the same ligand-exchange procedure as used in the TPC experiments. The measurements were performed under identical excitation conditions: 3.6-eV, 150-fs pump pulses at an average excitation level of $\langle N \rangle = 0.3$ and a pump–probe delay of $\Delta t = 4$ ps. In both samples, the band-edge bleach is centred at 2.35 eV, demonstrating that ligand exchange and film processing preserve the QD bandgap and, therefore, the quantum-confinement regime without evidence of QD sintering. The broader bleach observed in the film sample is attributed to the lower signal-to-noise ratio resulting from the much smaller optical density of the 200-nm film, which partially obscures the two closely spaced transitions involving the same $1S_e$ electron level and the $1S_{h,3/2}$ and $2S_{h,3/2}$ hole states.

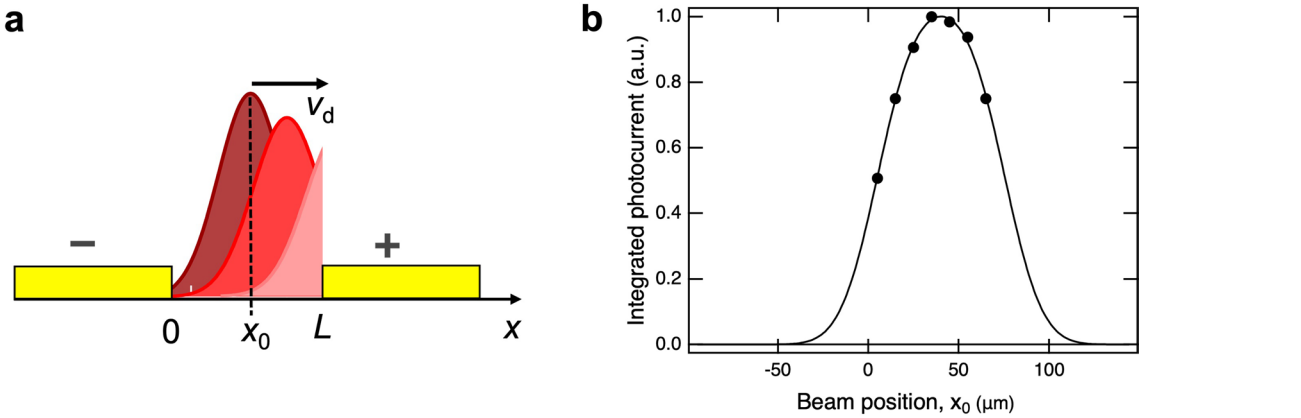

Extended Data Fig. 9 | Spatial profile of the hot-electron packet used for ToF modelling. a, Schematic of a TPC ToF experiment. A photoconductive gap is defined between two electrodes with edges at $x = 0$ and $x = L$. The centre of the focused laser beam is positioned at $x = x_0$. The photoinjected electron packet drifts towards the charge-collecting electrode with velocity v_d. **b**, Integrated photocurrent (circles) plotted as a function of the laser beam position (x_0) within the photoconductive gap. The data were obtained for a heavily doped Mn:CdSe/CdS QD film at an excitation level of $\langle N \rangle = 5.12$ excitons per dot per pulse (Supplementary Note 3). To exclude the initial spike arising from capacitive current, the integration window was restricted to 0.4–4.0 ns, corresponding to the dominant drift photocurrent component. The solid line is a fit using the model described by equation (S3.6) in Supplementary Note 3, from which the FWHM of the hot-electron packet is determined to be $\Gamma_{1/2,\mathrm{hot}} = 41.5$ μm. Consistent with the approximately cubic dependence of the hot-electron photocurrent on $\langle N \rangle$ (Fig. 2d, inset), this width is smaller than the original laser beam width (70–80 μm) by approximately a factor of $\sqrt{3}$. a.u., arbitrary units.